Influence of the PM-Processing Route and Nitrogen Content on the Properties of Ni-Free Austenitic Stainless Steel

KATHRIN LEFOR, M. WALTER, A. WEDDELING, E. HRYHA, S. HUTH, S. WEBER, L. NYBORG, and W. THEISEN

Ni-free austenitic steels alloyed with Cr and Mn are an alternative to conventional Ni-containing steels. Nitrogen alloying of these steel grades is beneficial for several reasons such as increased strength and corrosion resistance. Low solubility in liquid and δ-ferrite restricts the maximal N-content that can be achieved *via* conventional metallurgy. Higher contents can be alloyed by powder-metallurgical (PM) production *via* gas–solid interaction. The performance of sintered parts is determined by appropriate sintering parameters. Three major PM-processing routes, hot isostatic pressing, supersolidus liquid phase sintering (SLPS), and solid-state sintering, were performed to study the influence of PM-processing route and N-content on densification, fracture, and mechanical properties. Sintering routes are designed with the assistance of thermodynamic calculations, differential thermal analysis, and residual gas analysis. Fracture surfaces were studied by X-ray photoelectron spectroscopy, secondary electron microscopy, and energy dispersive X-ray spectroscopy. Tensile tests and X-ray diffraction were performed to study mechanical properties and austenite stability. This study demonstrates that SLPS process reaches high densification of the high-Mn-containing powder material while the desired N-contents were successfully alloyed *via* gas–solid interaction. Produced specimens show tensile strengths >1000 MPa combined with strain to fracture of 60 pct and thus overcome the other tested production routes as well as conventional stainless austenitic or martensitic grades.

DOI: 10.1007/s11661-014-2701-7

I. INTRODUCTION

STAINLESS steels are indispensable in industry and daily life. The production of 35.4 million tons of stainless steels in 2012 underlines their importance.[1] The dominant grades are stable austenitic steels. Onwards, CrNi grades represent about half of the produced stainless crude steel. Due to the high price of nickel and the classification as an allergy-inducing element, Ni-free austenitic grades on CrMn base become more important. The produced tonnage in 2012 constituted already 20 pct of stainless steel production.[1]

Nitrogen alloying of these steels is beneficial for several reasons. Nitrogen in solid solution is the most effective element to increase the strength of austenitic steel.[2] The yield and the tensile strength at room temperature increase linearly with nitrogen content in solid solution.[3,4] Since nitrogen is an austenite stabilizing element, it increases the resistance against undesired δ-ferrite and suppresses the formation of α-martensite during deformation.[3,5] Moreover, the addition of nitrogen to carbon leads to an increase of stability of homogeneous austenite.[6] Thus, even though the amount of interstitials increases by the addition of N, the solvus temperature of precipitates can be lowered.[7] Furthermore, it was shown that the combined alloying of carbon and nitrogen can increase the strength without the expected deterioration of toughness.[8–13] Thus, C + N-alloyed CrMn-austenitic steels feature outstanding mechanical properties combined with corrosion resistance, intensive cold work hardenability, and a heating resistance up to 773 K (500 °C).[14] Furthermore, the non-magnetic behavior makes this steel grade suitable for applications in environment of strong magnets as are present in magnetic resonance imaging or alternating electric fields.[14,15] Detailed information about the concept of combined alloying of C and N (C + N concept) and the influence of N on the mechanical properties can be extracted from.[8–13]

The steel investigated in this work Fe-19Mn-18Cr-0.4C-0.3N was developed in previous studies using the C + N concept. It was designed for ingot metallurgy under ambient pressure. As the N-solubility is low in liquid state and even lower in the δ-ferrite, the N-content was limited to ~0.6 mass pct,[16] even though the solubility of N in solid austenitic state is far higher. However, equilibrium calculations reveal that an increase of the nitrogen content to 0.825 mass pct results in an expansion of the austenite phase field toward lower temperatures (Figure 1), which lowers the equilibrium precipitation temperatures of nitrides and carbides and

KATHRIN LEFOR, M. WALTER, and A. WEDDELING, Researchers, S. HUTH and W. THEISEN, Professors, are with the Chair of Materials Technology, Ruhr-UniversitätBochum, Universitätsstraße 150, 44801 Bochum, Germany. Contact e-mail: Lefor@wtech.rub.de E. HRYHA, Researcher, and L. NYBORG, Professor, are with the Department of Materials and Manufacturing Technology, Chalmers University of Technology, Rännvägen 2A, SE-412 96 Gothenburg, Sweden. S. WEBER, Professor, is with the Chair of Novel Manufacturing Technologies and Materials, Bergische Universität Wuppertal, Bahnhofstr. 15, 42651 Solingen, Germany.

Manuscript submitted June 12, 2014.
Article published online December 17, 2014

thus the temperature for solution annealing. Furthermore, because precipitation starts at lower temperatures, a lower critical cooling rate is required to obtain a precipitate-free material leading to higher producible cross sections.[15,17]

This higher nitrogen content of 0.825 mass pct can be obtained if a powder-metallurgical (PM) production route is applied. During sintering under N_2 atmosphere, a gas–solid interaction results in a nitrogen uptake of the steel powder. Since the interaction takes place below the liquidus temperature, the higher solubility of the solid state can be exploited. The amount of absorbed nitrogen depends on the partial pressure of the nitrogen, alloy composition, and temperature. In case of the investigated steel the nitrogen dissolution was observed to start at about 973 K (700 °C).[18] Thus, besides the well-known positive effects of PM-production, as elimination of segregations and production of products with complex shapes with regard to economy of material and postprocessing,[19,20] powder metallurgy also offers the possibility of purposefully modifying the nitrogen content.

However, conventional solid-state sintering (SSS) of high alloyed steel is often impeded by its low sintering activity. Thus, for successful SSS pressure-assisted consolidation is preferred, *e.g.*, hot isostatic pressing (HIP). An alternative to the high-cost HIP process is the supersolidus liquid phase sintering (SLPS). During SLPS, loose powder mass is heated above the solidus but below the liquidus temperature in order to provide about 30 pct of liquid phase leading to a rapid densification.[21]

Nevertheless, the alloying with nitrogen and the substitution of Ni by Mn lead to processing challenges for PM-production. Nitrogen may degas and the high vapor pressure of Mn leads to its evaporation sublimation at temperatures above 973 K (700 °C) in high vacuum.[22–24] Another problem is the enclosure of the surface oxides in the developing inter-particle necks resulting in a decreased performance of sintered steel as they act as crack initiation sites. Whereas less stable oxides, like iron oxides, are reduced during the sintering cycle; the more thermodynamically stable Mn-rich oxides may become enclosed during consolidation. This is especially critical as they incline to transform into even more stable Si-containing mixed oxides above ~1073 K (~800 °C).[23]

For that reason, the parameters of the sintering process, such as the atmosphere and the temperature profile, have to be adapted to the material regarding both, the densification and the oxide reduction. This study investigates the influence of PM-processing route on the mechanical properties of sintered N-containing Ni-free austenitic stainless steel. Therefore, a prealloyed high-CrMn-steel powder is consolidated *via* different PM-processing routes. Three sintering routes are applied which are SSS, SLPS, and HIP. Sintering temperatures are determined by differential thermal analysis (DTA). The first two processing routes are performed under nitrogen atmosphere in order to increase the nitrogen content from the initial level of ~0.3 mass pct to 0.825 mass pct *via* gas–solid interaction. The required nitrogen partial pressure is obtained

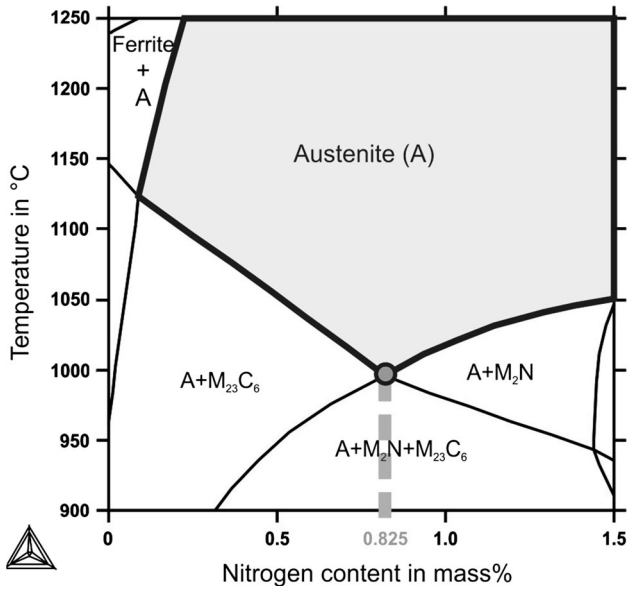

Fig. 1—Calculated phase diagram of the investigated steel as a function of nitrogen content. A N-content of 0.825 mass pct results in a maximal widening of the austenite phase field toward lower temperatures.

by means of thermodynamic calculation. Additionally, aspiring an improved oxide reduction during the sintering cycle, vacuum dwelling steps are introduced at different temperatures that are chosen based on former studies, literature review, and residual gas analyses (RGA).

Fracture surfaces are analyzed by X-ray photoelectron spectroscopy (XPS), and secondary electron microscopy (SEM) combined with energy dispersive X-ray spectroscopy (EDX). Tensile tests were performed to prove the beneficial influence of the evaluated parameters on mechanical properties. Afterward, the resistance against δ-ferrite and α-martensite is proven by means of X-ray diffraction (XRD) of highly strengthened area.

II. EXPERIMENTAL

A. *Material*

The powder was produced *via* gas atomizing of a prealloyed melt with nitrogen gas and sieved to a maximum diameter of 200 μm. The chemical composition was measured by optical emission spectrometry of a HIPed specimen and is listed in Table I.

B. *Design of Sintering Route*

In order to figure out optimal sintering parameters, the influences of the sintering temperature T_{sint} and of a vacuum dwelling step at two different temperatures T_{dwell} are investigated.

A vacuum dwelling step at 973 K (700 °C) prior to sintering was chosen because prior investigations reveal an optimum reduction of surface oxides and formation

Table I. Chemical Composition of the Investigated Steel as Measured by Optical Spark Emission Spectrometry of a Hipped Specimen

Element	C	Cr	Mn	Mo	N	Ni	Si	Fe
Mass pct	0.39	17.08	19.67	0.99	0.31	0.46	0.45	bal.
At pct	1.77	17.65	19.24	0.55	1.21	0.42	0.86	bal.

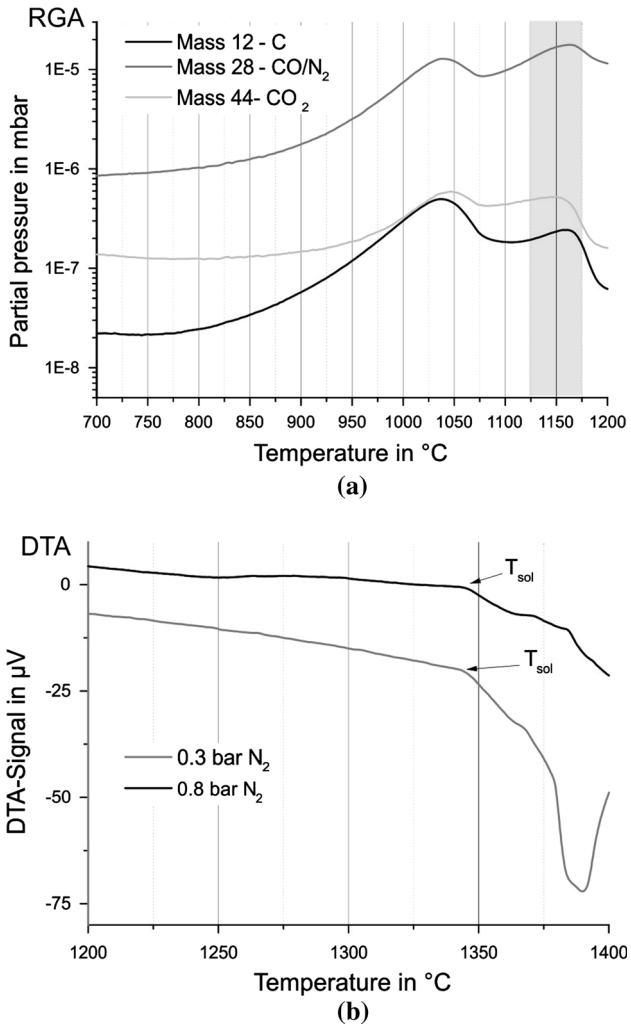

Fig. 2—(*a*) RGA-measurements revealing oxide reduction at ~1298 K (~1025 °C) and ~1423 K (~1150 °C) and (*b*) DTA measurements revealing a solidus temperature of ~1613 K (~1340 °C) if nitrogen is applied as sintering atmosphere. Data is extracted from.[27]

of sintering necks at relatively low temperatures when low vacuum is applied.[25,26] Moreover, Mn evaporation is calculated to strongly increase above 973 K (700 °C),[24] which is also supported by experimental investigations.[23] Additionally, a dwelling step at 1423 K (1150 °C) was performed because RGA, depicted in Figure 2(a),[27] revealed carbothermal reduction of surface oxides until this temperature in vacuum.

The sintering temperatures were chosen based on DTA measurements (Figure 2(b)) that reveal a solidus temperature (T_{sol}) of about 1618 K (1345 °C) under 0.3 and 0.8 bar of nitrogen.[27] A sintering temperature below (1613 K/1340 °C) and one above (1633 K/1360 °C) T_{sol} were chosen for SSS and SLPS, respectively.

The equilibrium nitrogen partial pressure required to achieve a nitrogen content of 0.825 mass pct at sintering temperatures was calculated as 0.175 MPa using the Calphad software ThermoCalc, version S with the database TCFe6.2 for iron-base systems.

C. *Sample Preparation*

Within the first batch of experiments (1st batch), the influence of the sintering temperature T_{sint} and the influence of an optional vacuum dwelling step at two different temperatures T_{dwell} on densification and fracture are investigated. Specimens are analyzed by chemical and microstructural analysis. Additionally, the fracture surfaces are investigated by XPS, SEM, and EDX. Afterward, the sintering parameters with the best outcome are used to produce specimens for tensile tests (2nd batch).

For the first sintering batch, about 60 g of powder was filled into an open corundum crucible (10 × 10 × 80 mm^3) and sintered in a vacuum furnace. The second sintering batch was performed using 1 kg of powder resulting in sintered blocks of 50 × 50 × 120 mm^3. The parameters of the applied sintering routes and sample abbreviations are given in Table II. The SSS^0 and SLPS samples were heated continuously up to 1613 K and 1633 K (1340 °C and 1360 °C), respectively, under the increased nitrogen partial pressure of 1.75 bar N_2. In case of SSS + 700, SSS + 1150, and SLPS + 700 vacuum dwelling steps are inserted at noted temperatures. The heating rate was set to 10 K/min. The HIPed specimen was consolidated at 1423 K (1150 °C) and 100 MPa for 4 hours. Because the HIP process requires encapsulation, the nitrogen content could not be increased during compaction.

Sintering was followed by solution annealing in all cases at 1473 K (1200 °C) for 30 minutes under an Ar atmosphere and subsequent water quenching according to Reference 12.

D. *Analysis of Microstructure*

The grain sizes were determined by image analysis of light optical microscope images using interactive camera tracking and the linear intercept method at a magnification of hundred and two hundred times, respectively. The volume fraction of inclusions and pores was determined by means of image analysis using SEM images in SE contrast. Prior to analysis, the specimens were ground and polished to a mirror finish. No etching was applied.

E. *Chemical Analysis*

The overall chemical composition of the specimens, with special focus on the Mn-content, was measured by optical spark emission spectrometry. The oxygen content of the consolidated and heat-treated specimens was

Table II. Sample Abbreviations and Used Sintering Parameters Within This Study

	1st Batch				2nd Batch	
	SSS^0	SSS + 700	SSS + 1150	SLPS	SLPS	SLPS + 700
Dwelling step						
T_{dwell} (K/°C)	—	973/700	1423/1150	—	—	973/700
atmosphere	—	~10 Pa	~10 Pa	—	—	~10 Pa
Time t_{dwell} (min)	—	7	30	—	—	30
Sintering						
T_{sint} (K/°C)	1613/1340	1613/1340	1613/1340	1633/1360	1633/1360	1633/1360
Atmosphere (MPa N_2)	0.175	0.175	0.175	0.175	0.175	0.175
Time t_{sint} (min)	360	360	360	120	120	120

Table III. Measured values for porosity/Inclusions and Grain Size (Image Analysis) and N—(Combustion Analysis), O—(Inert Gas Fusion Infrared Absorption Method), and Mn—(Optical Spark Emission Spectrometry) Contents

	HIP	SSS^0	SSS + 700	SSS + 1150	SLPS
Porosity/inclusions (pct)	0.7	12.3	11.2	19.5	1.2
Grain size (μm)	25	100	100	100	150
N-content (mass pct)	0.308	0.882	0.853	0.833	0.828
O-content (mass pct)	0.053	0.049	0.038	0.044	0.071
Mn-content (mass pct)	20.2	19.3	19.4	20.1	20.0

measured by an inert gas fusion infrared absorption method. Nitrogen was measured by combustion analysis.

F. *Analysis of Fracture Surfaces*

1. *XPS*

The XPS investigations were performed on fracture surfaces. Therefore, specimens ($4 \times 4 \times 10$ mm^3) were broken at room temperature in an extended vacuum chamber under a 10^{-5} Pa (UHV) vacuum, and the as-fractured state was analyzed under the same conditions. Ar ion beam-controlled etching was applied to remove materials gradually from the fracture surface up to a depth of 50 nm, followed by XPS analysis. Subsequently, the surface composition and metallic fraction were investigated by numerical fitting of high-resolution narrow scans of the characteristic XPS peaks.

2. *SEM + EDX*

The as-fractured surfaces of the specimens were investigated after XPS analysis using a high-resolution SEM in SE contrast mode. EDX analysis was performed using an EDX detector connected to the SEM chamber. Therefore, an acceleration voltage of 15 kV, a working distance of 8 mm, and a measurement time of 100 seconds were used.

G. *Analysis of Mechanical Properties*

The hardness values were determined according to DIN 17021-1 using a force of 294.2 N (HV30). Given values are the average values of five measurements. Tensile tests were carried out for specimens produced within the 2nd sintering batch at room temperature. The initial length was $l_0 = 17$ mm and the diameter $d_0 = 3$ mm. Tests were performed with a testing speed of 0.5 mm per minute (0.00049/s^{-1}) according to DIN EN 10002-1.

H. *Analysis of Austenite Stability*

X-ray diffraction analyses were carried out on the deformed tensile test specimens to investigate the possibility of strain-induced transformation of the austenite as well as to ensure no participation of ferrite takes place in the microstructure.

III. RESULTS

A. *First Sintering Batch*

1. *Analysis of microstructure*

The combined volumes of pores and inclusions are shown in Table III. This volume is determined to 0.7 pct in case of the HIPed specimen and 1.2 pct for the SLPS specimen. The SSS^0 specimen was measured to inhibit a significantly higher volume of pores and inclusions reaching about 12 pct, whereas this amount was slightly improved in the case of SSS + 700 (11 pct), but deteriorated significantly if a dwelling step at 1423 K (1150 °C) was applied (20 pct).

The grain size, see Table III, increases with increasing processing temperature and thus was the largest for the SLPS specimen with about 150 μm and the lowest for the HIPed specimen with 25 μm. The dwelling steps at 973 K (700 °C) and 1423 K (1150 °C) show no effect on the grain size, as the values for SSS + 700 and SSS + 1150 are similar to that of the SSS^0 specimen (100 μm).

2. *Chemical analysis*

The nitrogen content of the sintered specimens are measured to be increased from the initial value of ~0.3 mass pct to values between 0.828 and 0.882 mass pct (Table III). The Mn-content is close to the initial content for all investigated specimens. The measured oxygen content (Table III) of the HIPed specimen was

0.053 mass pct. The highest O-content was measured for the SLPS sample with 0.071 mass pct. The SSS^0 specimen shows with 0.049 mass pct a slightly lower oxygen content compared with HIP which is further reduced in SSS + 1150 to 0.044 mass pct and especially in SSS + 700 to 0.038 mass pct, which has the lowest oxygen content measured.

3. *Analysis of fracture surfaces*

a. XPS. Figure 3(a) shows the oxygen content measured on the fracture surfaces by XPS as a function of etch depth. The oxygen content is an indicator of the amount of oxides present on the fracture surface. It must be taken into consideration that the roughness of the fracture surface influences the tendency of the oxygen content development with etching depth due to the shadowing effects during Ar ion etching. XPS analysis indicates distinctly lower oxygen content in the HIP and SLPS specimens compared with the SSS specimens. Comparing only the SSS specimens, the SSS + 700 specimen show the lowest oxygen fraction and the SSS + 1150 specimen the highest.

Figures 3(b) through (f) show the relative cation concentrations of the elements in oxide state on the fracture surface. The relative cation concentration represents the fraction of the oxide state of each element in relation to all measured cations, thus providing information about the oxide composition. The diagrams reveal that the oxides present on the fracture surface are manganese based, irrespective of the processing route. The iron fraction, however, varies significantly. Whereas the iron fraction is negligible for HIP and SLPS, it is about 20 pct for SSS^0 and SSS + 700 and above 30 pct for the SSS + 1150 specimen.

Additionally, the narrow scan of the O_{1S} peak of the unetched surface is shown in Figure 4. The integrated peak intensity is related to the amount of oxygen present on the surface whereas the binding energy peak position correlates with the oxide phase formed. The peak situated at ~530 eV is related to metallic oxides such as Mn, Cr, or Fe oxides, whereas the peak at higher energies (~532 eV) is related to more stable Si-containing mixed oxides. It elucidates that the HIP and SLPS specimens have much lower oxygen content at the outermost fracture surface than SSS specimens. The double peak of SLPS and HIP specimens is clearly pronounced, which means oxygen is present in metallic-based and silicon-containing oxides in about equal amounts, whereas the amount of less stable oxides clearly dominates in case of all three SSS specimens.

b. SEM + EDX. Figure 5 shows an overview of the as-fractured surfaces of the different specimens as well as a close up in order to evaluate fracture mechanism and morphology of enclosed particulates. The fracture surfaces of the SLPS and HIP specimens show a high densification, whereas in case of the SSS specimens the pores can be seen. The fracture mode can be identified as dominantly inter- and trans-particle dimple rupture initiated by enclosed particulates. Compared with the other specimens the SLPS specimen exhibits larger dimples and large oxide residues.

In case of the HIPed specimen only spherically shaped particulates can be found (Figure 5(a)). This particulate morphology can also be observed in all SSS specimen (Figures 5(e) through (j)). The shape and size of most of the enclosed particulates in the SLPS specimen differ from those found in the HIP and SSS specimens: they are much bigger and rather angular (Figures 5(c) and (d)). They are located in larger dimples with more free metallic matrix between them. All SSS specimens also show a flaky layer inside their open pores as can be seen in Figure 5(h) for the SSS + 1150 specimen.

Ten particulates per sample were analyzed *via* EDX analysis. Reference measurements on oxide-free metallic fracture surface of each sample were performed additionally. Representative semi-quantitative EDX measurements and the related spots of measurements depicted on SEM micrographs are presented in Figure 6. EDX measurements show increased O, Mn, and Si contents for the majority of the measured enclosed particulates in case of all investigated specimens. Some particulates also show a contribution of the trace element Al.

B. *Second Sintering Batch*

1. *Selection of sinter parameters*

The SSS + 700 specimen does not only contain the lowest overall oxygen content, its oxide/oxygen fraction on the fracture surface is also the lowest for SSS and confirms the improved solid-state consolidation by annealing at 973 K (700 °C) in vacuum condition. However, pressureless SSS does not result in sufficient densification. Thus, even though SLPS results in the highest overall oxygen content (Table III) the oxygen fraction at the fracture surface is about the lowest of the investigated samples (Figures 3(a) and 4) and it results in a desirable high densification (Table III).

Based on the presented results, the combination of SLPS consolidation at 1633 K (1360 °C) under a nitrogen pressure of 1.75 bar and a vacuum dwelling step at 973 K (700 °C) for 30 minutes is further assumed to be the optimal sintering route. Since SLPS + 700 was not tested yet, two additional sintering experiments, SLPS and SLPS + 700 (Table II) were performed within the 2nd sintering batch in order to produce samples for tensile tests.

2. *Analysis of mechanical properties*

The hardness values are listed in Table IV. The obtained values for the SLPS-sintered materials are higher (~270 HV 30) compared with the HIPed specimen (256 HV 30). Comparing the SLPS-sintered materials, the sample SLPS + 700 shows a slightly higher hardness.

Tensile tests were carried out on each of the six specimens for SLPS-produced materials and four for the HIPed material. Representative stress–strain curves are depicted in Figure 7. The determined values are listed in

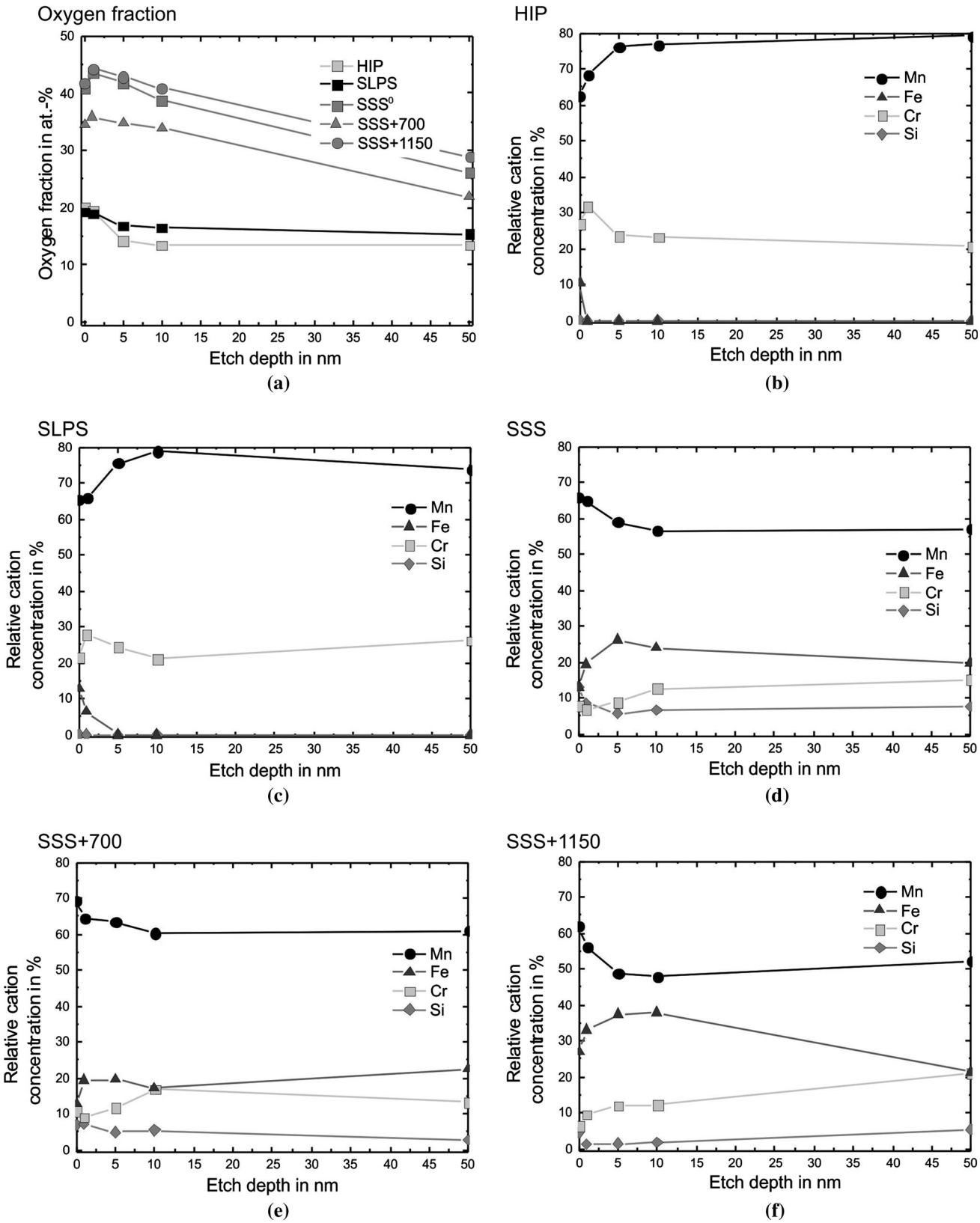

Fig. 3—XPS-analysis of fracture surfaces of investigated specimens as a function of etch depth. (*a*) oxygen fraction as a comparison of all specimens. (*b*) through (*f*): relative cation concentration of fracture surfaces.

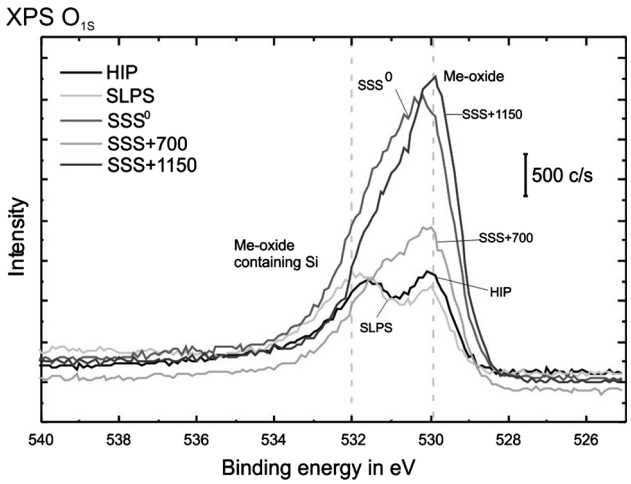

Fig. 4—Narrow scan of the O_{1s} oxygen peak of fracture surfaces revealing that specimens contain two types of oxides. The area under the graphs can be correlated to the amount of oxygen at the fracture surface.

Table V. It can be seen that two and three out of six specimens failed prematurely in case of both SLPS-sintered materials, SLPS and SLPS + 700. These samples are not considered for determination of characteristic values and denoted by an asterisk. The fracture of the prematurely failed samples always occurred close to the thread of the samples. Figure 8 shows a comparison of the fracture surfaces of a prematurely failed and a successfully tested specimen. It can be seen that the former one failed due to an area that was not consolidated (Figures 8(a) and (b)). In this area, non-sintered powder particles can clearly be seen (Figure 8). The position of these insufficiently densified areas allows to assume that within the edge area of the sintered block, the density is worse compared with the inner material leading to an increased porosity close to the thread of tensile specimen.

By means of the successfully tested specimen the average values of characteristic values of tensile tests are extracted (Table V). It can clearly be observed that the mechanical properties of the successfully sintered SLPS specimen overcome the HIP samples. Both, the yield strength and the tensile strength of the SLPS specimens are higher compared with values of the HIPed specimens. The fracture work W_s represents the combination of strength and toughness since it is the integrated stress–strain curve.[7] The values are significantly higher for the SLPS specimen (~523 J/cm^3) compared with HIP (~403 J/cm^3). It has to be noted that the addition of a dwelling step at 973 K (700 °C) further increases the observed values as the fracture work increases to ~548 J/cm^3.

3. *Analysis of the austenite stability*

XRD measurements, depicted in Figure 9, show that neither ferrite nor martensite is present in the fractured SLPS-produced samples and thus confirm a stable austenitic microstructure of the sintered material even after extensive strengthening. The HIPed specimen, however, shows a reflection that is related to ferrite or martensite. A differentiation between these two body cubic centered (bcc) phases is difficult due to very fine differences in reflex position but will be discussed later.

IV. DISCUSSION

A. *First Sintering Batch*

1. *Analysis of microstructure*

The measured combined value of 0.7 vol pct pores and inclusions in case of the HIP specimen can be concluded to represent solely the inclusions as a complete densification can be assumed after consolidation by HIP. The value of 1.2 vol pct for the SLPS specimen, sintered at 1633 K (1360 °C), is acceptably low. For specimens sintered at 1613 K (1340 °C) without presence of liquid phase the obtained values are significantly higher (11 to 20 vol pct), indicating that pressureless SSS does not lead to a sufficient densification in contrast to HIP and SLPS. Additionally, the use of a high temperature annealing step at 1423 K (1150 °C) did not lead to an improved consolidation but rather downgraded the sintering result, whereas a dwell at 973 K (700 °C) improved consolidation slightly.

2. *Chemical analysis*

The measured nitrogen contents reveal a good accordance to the desired content of 0.825 mass pct. It consequently can be concluded that the applied calculations by means of the Calphad method are appropriate for determination of nitrogen partial pressures for nitrogen alloying *via* gas–solid interaction of the investigated steel.

As experienced in former studies a heat treatment under high vacuum of about 10^{-3} Pa led to a progressive evaporation of Mn starting at 973 K (700 °C), which consequently restricts the usage of such high vacuum.[22,23] Within this series of experiments, however, the Mn-content indicates no evaporation of this element for all investigated specimens due to the lower vacuum levels applied.

Because the encapsulation does not allow any interaction with the atmosphere during HIP processing, the oxygen content of the HIPed specimen of 0.053 mass pct is regarded as the oxygen level of the powder material in the initial state. The oxygen content of the SLPS specimen is the highest measured within this study with 0.071 mass pct. Consequently, during sintering at 1633 K (1360 °C) and subsequent cooling an oxygen uptake must have occurred. On the contrary, the oxygen content of SSS^0 of 0.049 mass pct is about the initial state's content, which indicates that oxidation and reduction processes inside the furnace until 1613 K (1340 °C) under nitrogen atmosphere result neither in an increase nor in a significant decrease of the overall oxide content. The O-contents further show that an additional vacuum dwelling step prior to sintering leads to a decrease of oxygen content, since SSS + 700 and SSS + 1150 have lower O-contents than SSS^0. The vacuum dwelling step was applied based on the RGA

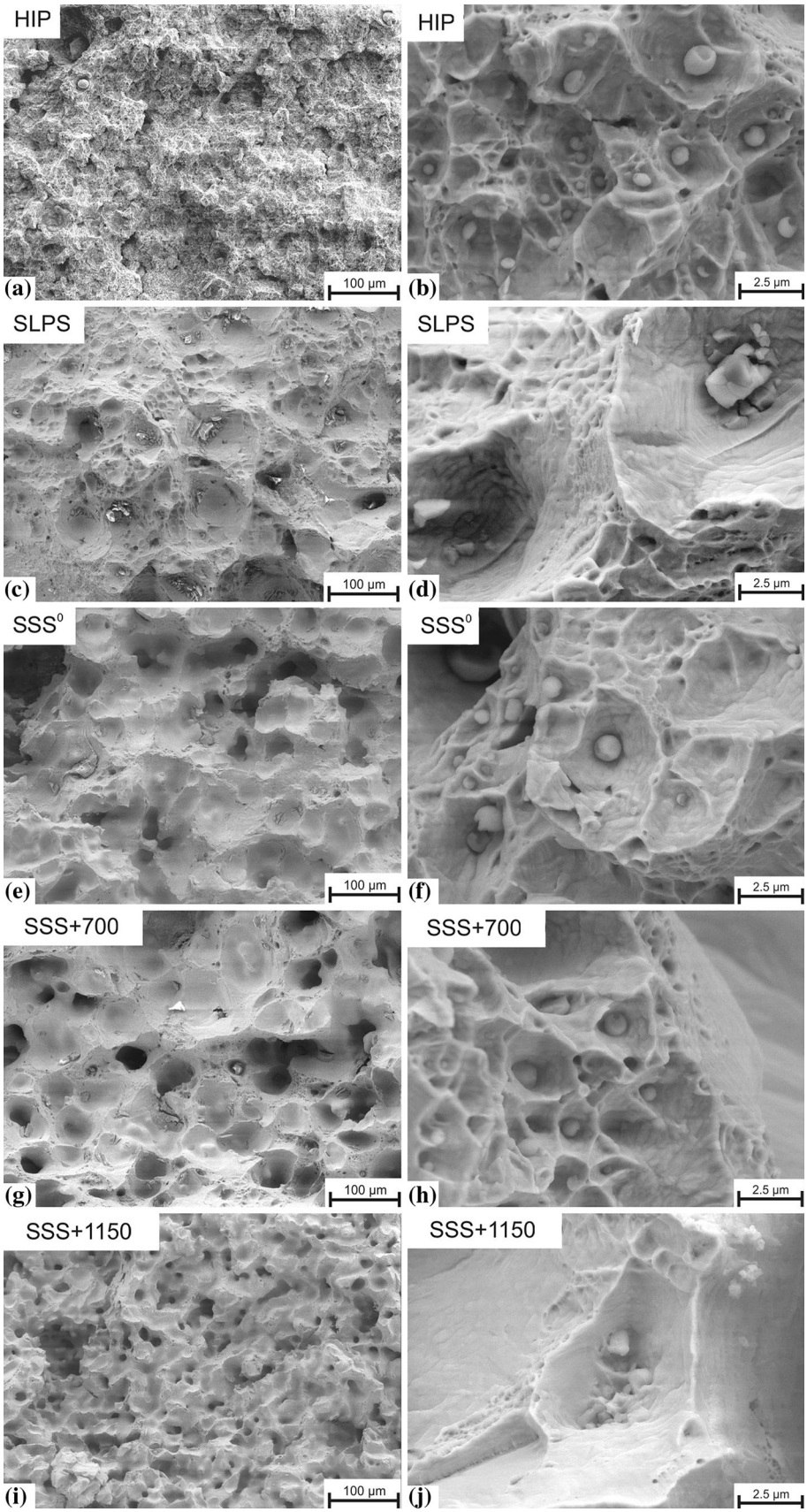

Fig. 5—SEM images of fractured surfaces of investigated specimens.

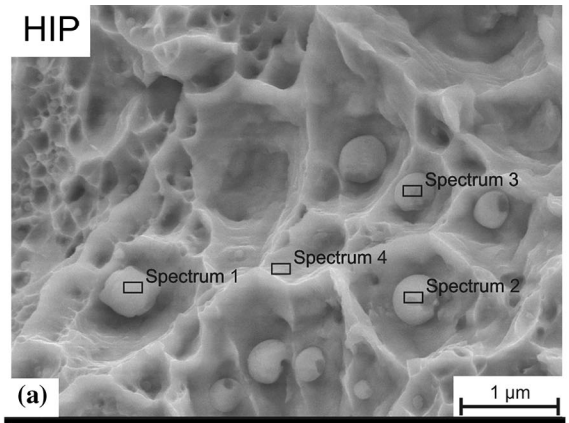

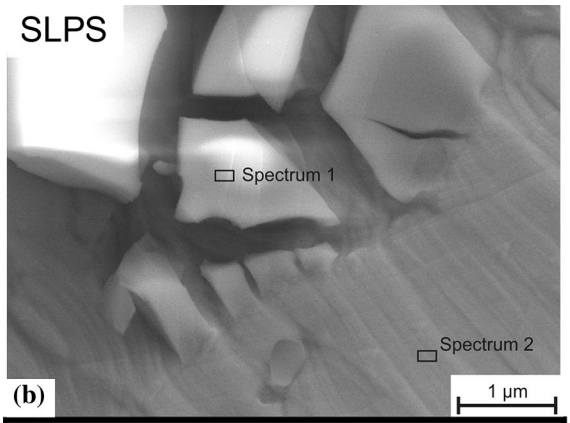

HIP - elements in at.-%

Sp.	N	O	Si	Cr	Mn	Al	Mo	Se	S	Fe
1	-	54.79	6.62	3.62	25.56	-	-	-	2.18	7.25
2	-	45.08	4.70	3.51	30.49	-	2.55	1.76	2.94	8.98
3	-	42.39	4.81	6.08	24.95	1.91	2.74	1.55	-	15.60
4	-	-	-	20.48	19.93	-	-	-	-	59.59

SLPS - elements in at.-%

Sp.	N	O	Si	Cr	Mn	Al	Mo	Se	S	Fe
1	-	30.97	8.35	2.30	48.53	1.64	1.75	1.24	-	5.22
2	5.02	-	-	18.33	20.25	-	-	-	-	56.40

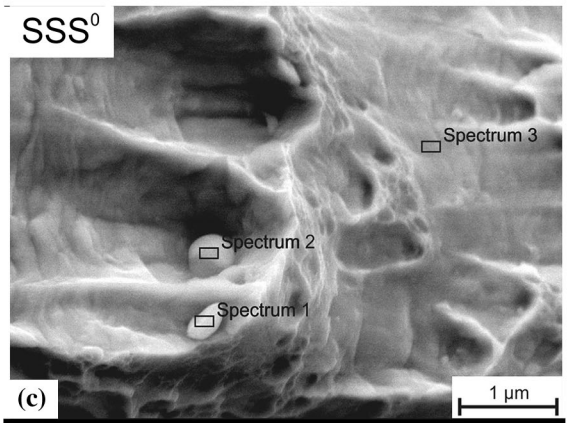

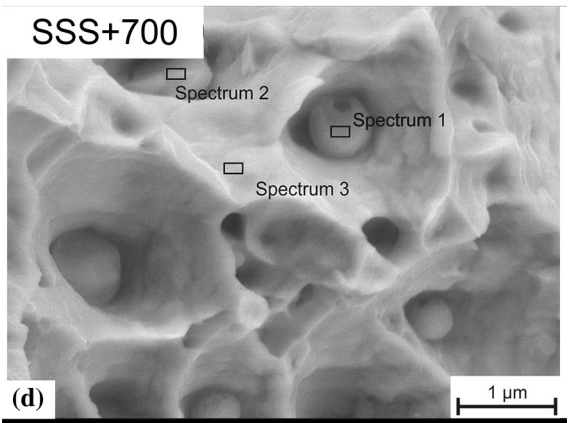

SSS^0 - elements in at.-%

Sp.	N	O	Si	Cr	Mn	Al	Mo	Se	S	Fe
1	-	8.2	-	7.42	33.88	2.39	8.10	8.39	8.39	19.96
2	-	54.42	0.92	4.46	15.96	14.81	-	1.34	1.34	8.09
3	3.45	-	1.02	18.33	18.30	-	0.96	-	-	57.94

SSS+700 - elements in at.-%

Sp.	N	O	Si	Cr	Mn	Al	Mo	Se	S	Fe
1	-	41.38	5.51	5.75	31.25	-	1.40	0.92	1.09	12.71
2	-	53.13	4.59	5.00	18.01	6.89	0.67	-	-	11.73
3	-	-	-	19.45	19.65	-	-	-	-	60.90

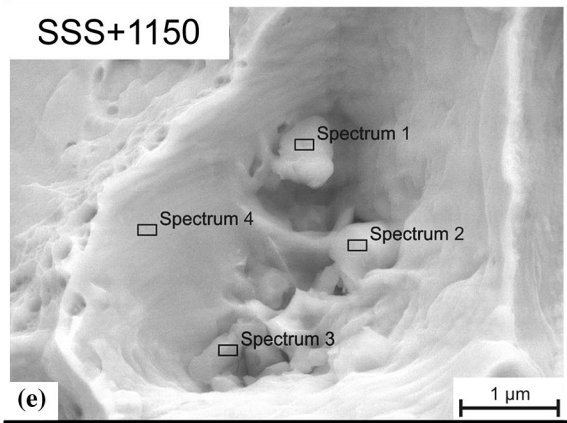

SLPS+1150 - elements in at.-%

Sp.	N	O	Si	Cr	Mn	Al	Mo	Se	S	Fe
1	5.05	61.02	-	2.29	9.77	15.81	-	-	-	3.90
2	6.74	57.68	-	4.29	7.82	12.52	-	-	-	3.98
3	-	55.87	-	4.78	11.15	17.42	-	-	-	10.00
4	3.31	-	-	18.34	19.11	1.26	-	-	-	57.99

Fig. 6—Quantitative results of representative EDX measurements and related spots of measurements.

Table IV. Hardness Values of Sintered Materials

	Hardness (HV 30)	Standard deviation
HIP	255.7	5.0
SLPS	269.3	3.5
SLPS + 700	272.8	6.8

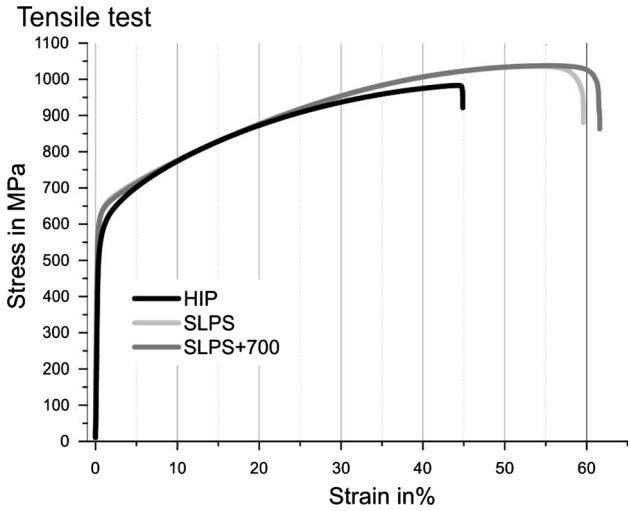

Fig. 7—Representative stress–strain curves of successfully tested specimens produced within the second sintering batch.

analysis depicted in Figure 2(a). Thus, the sintering route was optimized successfully. As described in,[28] sintering under vacuum leads to a favorable microclimate inside the powder mass during sintering, resulting in better conditions for a carbothermal reduction of iron oxides and thus in enhanced formation of sintering necks at temperatures well below sintering temperature. This mechanism is assumed to be responsible for the improved sintering results of SSS + 700 and SSS + 1150. Comparing both, a vacuum dwelling step at 973 K (700 °C) is more effective than a dwelling step at 1423 K (1150 °C). This is due to the improved diffusion of substitutional elements at higher temperatures which can lead to oxidation processes of elements with high oxygen affinity like Mn, Cr, and Si.

3. *Analysis of fracture surface*

a. XPS. The increased fraction of iron cations (Figures 3(b) through (f)) for all three solid-state sintered specimen indicates a higher amount of iron present in oxide compounds, whereas this value is negligible in case of HIP and SLPS specimen. Because the specimens were heat-treated at temperatures of 1613 K (1340 °C) and above, iron oxides are expected to be reduced during sintering as they are not thermodynamically stable at these temperatures. Consequently, the presence of iron oxide, as shown by the cation concentration,

Table V. Results of Tensile Tests

	Yield Strength $R_{p0.2}$ (MPa)	Tensile Strength R_m (MPa)	Uniform Strain A_g (pct)	Elongation to Rupture A (pct)	Fracture Work W_s (J/cm^3)
HIP#1	529	983	43.6	44.3	384.8
HIP#2	542	987	43.3	43.9	381.4
HIP#3*	528	977	43.9	44.8	386.0
HIP#4	534	988	48.4	52.1	461.2
Average value	**533**	**984**	**44.8**	**46.3**	**403.3**
Standard deviation	**5.5**	**4.3**	**2.1**	**3.4**	**33.4**
SLPS#1**	577	750	10.3	12.4	not calculated
SLPS#2	602	1040	53.0	59.2	543.6
SLPS#3	586	1020	55.2	60.7	548.2
SLPS#4	591	1020	49.8	52.5	468.4
SLPS#5*	596	1030	52.5	58.2	531.5
SLPS#6**	602	1040	16.0	19.9	not calculated
Average value	**594**	**1028**	**52.6**	**57.7**	**522.9**
Standard deviation	**5.9**	**8.3**	**1.9**	**3.1**	**320.7**
SLPS + 700#1**	582	931	32.2	34.3	not calculated
SLPS + 700#2	596	1050	56.0	65.1	564.6
SLPS + 700#3**	472	508	0.6	3.2	not calculated
SLPS + 700#4**	582	993	40.5	42.2	not calculated
SLPS + 700#5*	600	1040	55.1	61.2	610.7
SLPS + 700#6	597	1020	48.9	52.3	468.4
Average value	**598**	**1037**	**53.4**	**59.6**	**547.9**
Standard deviation	**1.7**	**12.5**	**3.2**	**5.4**	**592.7**

Bold values are the average values and their standard deviations.
*Depicted in Fig. 7.
**Unsuccessful trial, not considered for evaluation of the average value.

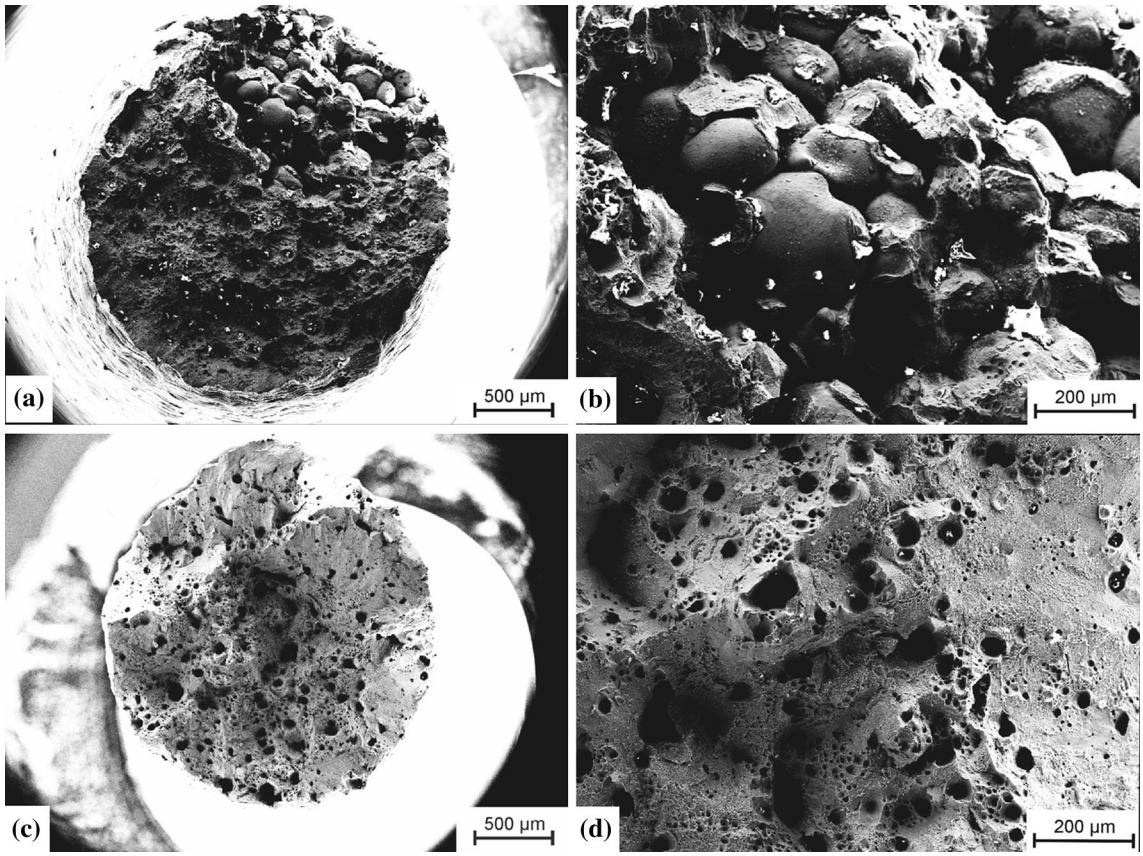

Fig. 8—SEM images of a prematurely failed (*a*) and a successfully tested (*c*) specimen. The close-ups show an insufficiently compacted area (*b*) compared with ductile fracture (*d*).

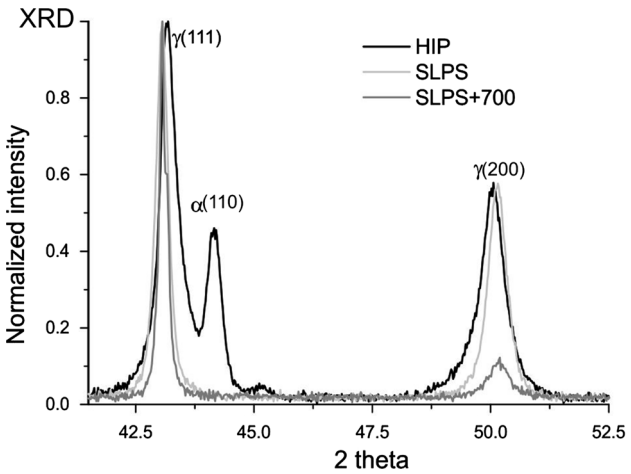

Fig. 9—XRD analysis of tested tensile specimens showing martensite formation (α) in the strengthened HIP specimen and a fully austenitic (γ) microstructure of the strengthened SLPS-sintered specimens.

results from reoxidation in pores during cooling and handling. As Chawla and Deng state in[29] the porosity tends to be interconnected if it exceeds about 5 vol pct, which is the case for the SSS specimens. Thus, it can be assumed that the iron oxide is an indicator for open porosity that is present in the solid-state sintered specimens. In this context, the highest iron fraction found in the SSS + 1150 specimen indicates a higher amount of open porosity compared with SSS and SSS + 700 specimens. These results are in agreement with the measured porosity/inclusion values (Table III) and the oxygen fraction at the surface (Figure 3(a)). Since pores, especially interconnected pores, deteriorate the performance of sintered steel[29] a sintering temperature of 1613 K (1340 °C) is consequently not advisable. The iron fraction in the relative cation concentrations is necessarily accompanied by a decrease in the Mn and Cr fractions. The evaluation of the slope of the narrow scan of oxygen, depicted in Figure 4, provides further evidence that the SSS specimens have a higher amount of oxides than SLPS and HIPed specimens and that the dwelling step at 973 K (700 °C) reduces the O-content clearly. The peak of the less stable oxides (~530 eV) dominates for the SSS specimens and is assumed to be mainly due to Fe-based oxides as a result of the reoxidation. Furthermore, a comparison of the oxygen peaks of SSS specimens indicates that heat treatment up to 973 K (700 °C) in vacuum is favorable.

b. SEM + EDX. The fracture surfaces of the HIP and SLPS samples (Figures 5(a/b) and (c/d)) confirm the high densification that is reached by these consolidation routes (compare Table III). The fracture surfaces of the SSS specimens reveal a high amount of porosity which is in accordance with the former results. This is known to

decrease the yield and tensile strength as well as ductility compared with a dense specimen as the load must concentrate at the sintering necks.[29] The mechanical properties of the SSS specimens are consequently supposed to be significantly worse than those of HIP and SLPS. The performance is further known to be deteriorated by defects situated at the sintering necks,[30] even though N. Chawla states that the effect of inclusions is minor if pore size is much larger than inclusion size.[29] Since the encountered dimple rupture is mainly initiated at a priori defects as pores, cracks, and inclusions,[31] the performance of the steel is expected to increase with increased consolidated area between those defects. The vacuum dwelling step at 973 K (700 °C) is therefore supposed to have a positive effect.

The flaky layer found on the pore surfaces of the SSS specimens is suggested to be iron-based oxides that form during cooling and handling of the samples within the open porosity. Their presence was already predicted based on the high amount of metallic-based oxides as shown by the oxygen narrow scan at ~532 eV (Figure 4). The presented EDX results indicate that the particulates present in the HIP, SSS, and the SLPS specimens are of oxidic character and feature about similar chemical compositions independently from consolidation route. EDX measurements also indicate a silicon fraction, which suggest that most obtained oxides are thermodynamically very stable Mn-Cr-Si oxides which are in agreement with previous investigations[23] and literature.[32] The Si fraction could not be measured accurately by XPS because the oxide content on the fracture surface of the specimens is rather low and thus the silicon peak was too small to be fitted accurately. The Al-content which is measured to be relatively high in some oxides is suggested to partially result from the used crucible that was composed of corundum. It has to be noted that the chemical composition of the agglomerates found in the SLPS specimen does not differ from the spherical oxides. It is thus concluded that the oxide particulates in the SLPS specimen are redistributed by the liquid phase resulting in oxide agglomerates. As the liquid phase forms primarily at the same sites as the oxides are located, oxides are assumed to be condensed by the melt. This alters the oxide distribution from a fine disperse arrangement to a minor number of coarser oxides. For that reason, the SLPS specimen shows a higher fraction of oxide-free matrix areas with pronounced ductility of the base matrix (Figures 5(b/c)).

B. *Second Sintering Batch*

1. *Mechanical properties and austenite stability*

The comparison of the results of the hardness measurement and tensile tests of the SLPS-, SLPS + 700-sintered, and HIPed specimens (Tables IV and V) clearly shows the high potential of the SLPS process as all obtained values of the specimens produced *via* SLPS overcome those of the HIPed material (Figure 7; Tables IV and V).

The results of hardness measurement and tensile tests are related to each other as they depend on the strength of the material.[33] In general a smaller grain size is related to the grain boundary hardening and result in an increase of hardness and yield strength (Hall–Petch equation). However, even though the SLPS specimen features a larger grain size of (150 μm) compared with the HIPed specimen (50 μm) it shows higher hardness and strength. This can be related to the increased nitrogen content of the SLPS and SLPS + 700 specimens. As Hänninen *et al*. compiled in[3] based on several references, the hardness as well as the yield and tensile strength at room temperature increase linearly with increasing N-content. This can be explained by solid solution hardening and by an increase of grain boundary hardening with increasing N-content.[3]

The comparison between SLPS and SLPS + 700 shows that even higher values of hardness, tensile strength, and strain values can be reached if a vacuum dwelling step is inserted in the processing route. This outcome confirms best densification if SLPS is applied in combination with a vacuum dwelling step. This must be related to a decrease of porosity and/or inclusions and thus to an optimization of production route if a dwelling step is applied as was already predicted by the results of the first sintering batch.

SLPS + 700 reaches a yield strength of 598 MPa, a tensile strength of 1037 MPa combined with a strain to fracture of ~60 pct, and a uniform elongation of ~53 pct. Thus, the investigated sintered CrMn austenite reaches yield and tensile strength comparable to conventional hardened and tempered stainless martensitic grades as 1.4021 ($R_{p0,2}$: ~600 MPa, R_m: ~850 to 950 Mpa) or 1.4122 ($R_{p0,2}$: ~550 MPa, R_m: ~750 to 950 MPa), while the toughness is significantly higher as martensitic steels feature uniform elongation of about 10 to 15 pct. Furthermore, compared with a standard CrNi-austenitic stainless steel (1.4301), that features a tensile strength of 500 to 700 MPa and an elongation to fracture of about 45 pct, the superior performance of the designed and produced CrMn steel becomes obvious.

XRD measurements of the SLPS and SLPS + 700 specimens show high degree of strain hardening without martensite transformation under mechanical load. The XRD measurement of the HIP sample, however, shows a reflex that can either be related to ferrite or strain-induced martensite. Since the initial powder is investigated to be nearly free from ferrite[18] and the chemical composition cannot be altered during HIP process, it is concluded that the reflection is related to strain-induced martensite. Thus, the increased nitrogen content of the SLPS-produced samples stabilizes the austenitic phase effectively, whereas the initial nitrogen content present in the HIP sample is not sufficient. This outcome is of importance regarding close-dimensional tolerances and the absence of ferromagnetic phases after high work hardening and once more highlights the potential of nitrogen alloying *via* gas–solid interaction. It even shows the potential to manipulate the strength by cold work hardening without unwanted phase transformation.

This amazing combination of properties makes the steel suitable for demand profiles that can neither be achieved by conventional stainless austenitic steel due to their insufficient strength nor by martensitic steels due to their low ductility. Additionally, this study proved that the material can undergo subsequent processing or

mechanical load during application involving high grades of strengthening without danger of martensite formation. Fields of applications for these PM-CrMn steels with increased N-content can be small devices with complex shapes in the vicinity of strong magnets that are needed to keep their non-magnetic behavior even under load and strengthening as necessary, *e.g.*, in medical engineering. Another field of application can be in corrosive environment with exposure to temperatures up to 773 K (500 °C) as in pumps or engines.

Thus, the results show that SLPS of the investigated steel under nitrogen atmosphere inhibits the potential to increase strength and toughness if compared with HIP production. The number of samples that fail prematurely, however, shows further necessity for improvement of the SLPS process.

V. SUMMARY AND CONCLUSIONS

Different PM densification techniques were applied to compact a high-CrMn-austenitic steel powder and to increase its nitrogen content by means of a gas–solid interaction. The results of this study lead to the following conclusions:

- Gas–solid interaction during sintering can be used to successfully adjust the nitrogen content of high-Mn-austenitic stainless steel powders. Hence, higher nitrogen contents can be alloyed compared with casting.
- Thermodynamic calculations by the Calphad method are an appropriate tool to obtain the required nitrogen partial pressure.
- The SLPS process leads to good densification, whereas solid-state sintered specimens are highly porous.
- The application of a vacuum dwelling step at 973 K (700 °C) improves consolidation and lowers the oxide content, which can be explained by the reduction of iron oxides.
- Successfully compacted SLPS-sintered specimen features a higher hardness and overcomes HIPed specimen in tensile tests concerning strength and ductility.
- Tested material featured yield strength of almost 600 MPa, a tensile strength of more than 1000 MPa combined with a uniform strain of more than 50 pct, and thus overcome conventional martensitic and austenitic stainless steel.
- Increased nitrogen content of SLPS-produced samples ensures austenite stability despite they having reached high values for elongation to fracture of more than 60 pct.

VI. OUTLOOK

The performed tensile tests yield prematurely fractured specimens due to bigger areas in the SLPS-sintered block that are not densified. This effect is assumed to be restricted to the edge areas of the sintered blocks as it is the case in this study. This assumption has to be proved.

Detailed information about the interaction between nitrogen content, mechanical and physical properties within the nitrogen-induced change in the atomic structure will be published in a future article.

ACKNOWLEDGMENTS

The authors gratefully acknowledge financial support from the Deutsche Forschungsgemeinschaft within the project TH 531/8-2. Special thanks go to Mr. Urban Jelvestam for his assistance and for performing the majority of the XPS analyses and to Dipl.-Ing. Michael Blüm for performing the sintering cycles.

REFERENCES

1. International Stainless Steel Forum: *Stainless Steel in Figures 2013*, 2013.
2. H. Berns and W. Theisen: *Eisenwerkstoffe: Stahl und Gusseisen*, 4th ed., Springer, Berlin, 2008.
3. H. Hänninen, J. Romu, R. Ilola, J. Tervo, and A. Laitinen: *J. Mater. Process. Technol.*, 2001, vol. 117 (3), pp. 424–30.
4. V. Gavriljuk, H. Berns, C. Escher, N. Glavatskaya, A. Sozinov, and Y. Petrov: *Mater. Sci. Eng., A*, 1999, vol. 271 (1–2), pp. 14–21.
5. T. Biggs and R.D. Knutsen: *J. Phys. IV France*, 1995, vol. 05 (C8), pp. 515–20.
6. L. Mújica Roncery: Doctoral Thesis, Bochum, Germany, 2010.
7. H. Berns and V.G. Gavriljuk: *KEM*, 2007, vols. 345–346, pp. 421–24.
8. V. Gavriljuk, B. Shanina, and H. Berns: *Acta Mater.*, 2000, vol. 48 (15), pp. 3879–93.
9. V.G Gavriliuk, B. Shanina, A. Tyshchenko, H. Berns, and S. Riedner: *Proc. of 10th Int. Conf. High Nitrogen Steels (HNS 09)*.
10. V. Gavriljuk, B. Shanina, and H. Berns: *Acta Mater.*, 2008, vol. 56 (18), pp. 5071–82.
11. H. Berns, S. Riedner, and A. Tyshchenko: *MSF*, 2007, vols. 539–543, pp. 4956–61.
12. S. Riedner: Doctoral Thesis, Bochum, Germany, 2010.
13. V.G. Gavriliuk and H. Berns: *High Interstitial Stainless Austenitic Steels*, 2012.
14. S. Riedner, H. Berns, A.I. Tyshchenko, V.G. Gavriljuk, C. Schulte-Noelle, and W. Trojahn: *Mat.-wiss. u. Werkstofftech.*, 2008, vol. 39 (7), pp. 448–54.
15. H. Berns, V. Gavriljuk, and B. Shanina: *Adv. Eng. Mater.*, 2008, vol. 10 (12), pp. 1083–93.
16. S. Riedner, N. Nabiran, and H. Berns: *Proc. 10th Int. Conf. High Nitrogen Steels (HNS 09)*, pp. 156–61.
17. H. Berns, S. Riedner, and V.G Gavriliuk: *Proc. 10th Int. Conf. High Nitrogen Steels (HNS 09)*, pp. 140–49.
18. K. Zumsande, N. Krasokha, S. Huth, S. Weber, and W. Theisen: *J. Mater. Sci.*, 2012, vol. 47 (7), pp. 3214–26.
19. P. Lindskog: *Powder Metall.*, 2004, vol. 47 (1), pp. 6–9.
20. W. Schatt, K.-P. Wieters, and B. Kieback: *Pulvermetallurgie: Technologien und Werkstoffe*, 2nd ed., Springer, Berlin, 2007.
21. R.M. German: *Sintering Theory and Practice*, Wiley, New York, 1996.

22. A. Weddeling, K. Zumsande, E. Hryha, S. Huth, and S. Weber: *Proc. Euro PM2011 Congr Exhib.*, 2011, vol. 2, pp. 15–20.
23. K. Zumsande, A. Weddeling, E. Hryha, S. Huth, L. Nyborg, S. Weber, N. Krasokha, and W. Theisen: *Mater. Charact.*, 2012, vol. 71, pp. 66–76.
24. E. Hryha and E. Dudrova: in *Application of Thermodynamics to Biological and Materials Science*, InTech, ed., pp. 573–602.
25. H. Borgström and L. Nyborg: *Powder Met.*, 2006, vol. 49 (1), pp. 48–56.
26. D. Chasoglou, E. Hryha, and L. Nyborg: *Powder Metall. Prog.*, 2009, vol. 9 (3), pp. 141–55.
27. N. Krasokha: Dissertation, Bochum, Germany, 2012.
28. D. Chasoglou: Dissertation, Gothenburg, Sweden, 2012.
29. N. Chawla and X. Deng: *Mater. Sci. Eng., A*, 2005, vol. 390 (1–2), pp. 98–112.
30. L. Čiripová, E. Hryha, E. Dudrová, and A. Výrostková: *Mater. Des.*, 2012, vol. 35, pp. 619–25.
31. E. Dudrova and M. Kabátová: *Powder Metall. Prog.*, 2002, vol. 8 (2), pp. 59–75.
32. R. Oro, M. Campos, E. Hryha, L. Nyborg, and J. Torralba: in *Proc. Euro PM2011 Congr. Exhib. 2011*, European Powder Metallurgy Association, ed., 2011, vol. 1, pp. 113–18.
33. F. Pöhl, S. Huth, and W. Theisen: *J. Mech. Phys. Solids*, 2014, vol. 66, pp. 32–41.